aerospace

MDPI

Article

Study on the Influence of Suction Parameters on the Effectiveness of Hybrid Laminar Flow Control for Two-Dimensional Airfoils

Ce Zhang, Hexiang Wang, Daxin Liao, Dawei Liu, Xiping Kou, Siyuan Gao, Guoshuai Li and Yang Tao *

High-Speed Aerodynamic Institute, China Aerodynamics Research and Development Center, Mianyang 621000, China; zhangce113@126.com (C.Z.); 15604125529@163.com (H.W.); daxinliao@mail.nwpu.edu.cn (D.L.); liudawei@mail.ustc.edu.cn (D.L.); kouxiping@cardc.cn (X.K.); gsy1999@nuaa.edu.cn (S.G.); gli221132@126.com (G.L.)

* Correspondence: taoyang@cardc.cn

Abstract

Boundary layer suction is a critical technique in hybrid laminar flow control (HLFC) for delaying transition and reducing drag. While the effectiveness of suction is well-established, systematic studies on the parametric optimization of suction hole diameter, location, and coefficient for two-dimensional airfoils remain scarce. This study addresses this gap through numerical investigations using the validated γ-$\widetilde{Re}_{\theta t}$ transition model. The research systematically analyzes the synergistic effects of suction coefficient (C_q), location (5%, 10%, and 15% chord), and suction hole diameter (0.2 mm, 0.6 mm, and 1.0 mm) on transition characteristics and aerodynamic performance. The results reveal that suction location predominantly governs the viscous drag coefficient (C_{Dv}), whereas suction hole diameter primarily influences the pressure drag coefficient (C_{Dp}). Consequently, suction location selection proves more critical for drag reduction than suction hole diameter. The maximum drag reduction (11.9% decrease in C_D) and optimal transition delay (11.8% chord shift) are achieved using a small suction hole (0.2 mm) located at an aft position (15% chord) with a high suction coefficient. Furthermore, an optimal matching range exists between suction location and coefficient, which widens with decreasing suction hole diameter. Based on these findings, this study proposes an energy-efficient design strategy: employing small apertures across the suction region while gradually increasing suction rates toward the trailing edge to achieve significant drag reduction with minimal energy penalty.

Keywords: hybrid laminar flow control (HLFC); γ-$\widetilde{Re}_{\theta t}$ transition model; suction control; transition; optimization

Check for updates

Academic Editor: Bosko Rasuo

Received: 16 April 2026
Revised: 15 May 2026
Accepted: 16 May 2026
Published: 19 May 2026

Copyright: © 2026 by the authors. Licensee MDPI, Basel, Switzerland. This article is an open access article distributed under the terms and conditions of the Creative Commons Attribution (CC BY) license.

1. Introduction

The hybrid laminar flow control (HLFC) technology is primarily applied to aircraft cruise conditions, with its primary objective being to reduce friction drag by sustaining laminar flow within the boundary layer. In modern aviation engineering, reducing the aerodynamic drag of aircraft is the core research direction to improve fuel efficiency and endurance performance [1–3]. According to Abbas et al. [4], for large transport aircraft in cruise condition, the total drag is mainly composed of friction drag (approximately 47%) and induced drag (approximately 43%). This drag breakdown highlights that focusing on skin friction reduction and lift-induced drag control is the most effective way to improve

overall aerodynamic performance. Since the skin friction drag of a laminar boundary layer is significantly lower than that of a turbulent boundary layer, extending the laminar region and delaying transition through boundary layer control techniques have remained focal points in aerodynamic design research. In recent years, strategic initiatives such as Flight Path 2050 [5] and Clean Sky 2 [6], which emphasize green aviation, energy conservation, and emission reduction, have further intensified global research interest in boundary layer control [7–10]. As a representative laminar flow control technique, boundary layer suction effectively delays transition and achieves substantial drag reduction by modifying the boundary layer velocity profile and suppressing disturbance growth, making it widely adopted in HLFC systems.

According to boundary layer flow stability theory, wall suction, favorable pressure gradient, and wall cooling constitute the three core mechanisms for enhancing boundary layer stability. Given the engineering impracticality of wall cooling in practical aircraft applications, the combination of suction and favorable pressure gradient has become the most widely adopted technical pathway for HLFC [11,12]. For two-dimensional airfoil flows, the chordwise pressure gradient directly determines laminar boundary layer stability: In favorable pressure gradient regions, the velocity profile exhibits no inflection point, allowing the laminar flow to remain stable. Upon entering adverse pressure gradient regions, the inflection-point velocity profile induces laminar flow instability and triggers the Tollmien–Schlichting (T-S) disturbance transition [13], as shown in Figure 1. Boundary layer suction delays transition by removing low-momentum fluid near the wall to improve the velocity profile and reduce disturbance growth rates. Consequently, precise matching of suction parameters with flow conditions is critical for the successful implementation of this technique [14,15].

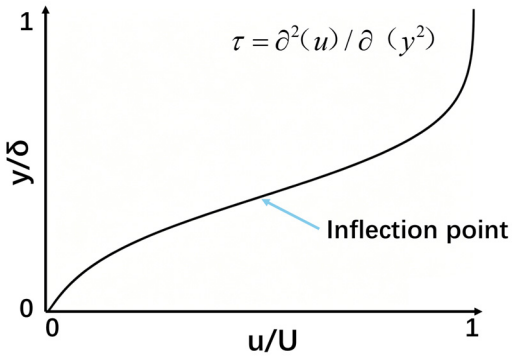


Figure 1. Schematic of velocity profile in the adverse pressure gradient region showing the inflection point.

Early research primarily validated the drag reduction effect of HLFC through wind tunnel tests [16]. In 1999, Schmitt et al. [17] conducted an HLFC vertical tail flight test based on the A320, maintaining an extensive stable laminar flow region on the vertical tail surface. Geng et al. [18] performed two-dimensional airfoil HLFC experiments in a low-turbulence wind tunnel, demonstrating that properly matched suction parameters could delay the transition location from 40% chord to beyond 80% chord, achieving significant drag reduction. The dimensions of the three suction apertures studied in this paper were also set based on Ref [18]. Wang et al. [19] investigated HLFC on a swept wing, finding that standard suction rates delayed transition to 80% chord, while double suction rates maintained laminar flow up to 85% chord, verifying the suppression effect of leading-edge suction on disturbance growth. Shi et al. [20] calibrated the equivalence between discrete-hole suction velocity and continuous-wall suction velocity in transonic wind tunnel tests. They validated the accuracy of coupling e^N transition prediction with RANS solvers for HLFC (transition pre-

diction error within 4% chord) and analyzed the suppression of crossflow vortices by wall suction alongside the negative impacts of wall blowing. P. Scholz et al. [21] tested a 1:0.7 scale vertical tail model (total height 4.45 m) in the DNW-LLF large low-speed wind tunnel under A320 cruise conditions. By integrating the Tailored Skin Single Duct (TSSD) suction system into the leading-edge region, they verified the engineering feasibility of TSSD, addressing key challenges of traditional active laminar flow control systems, including scalability limitations and poor maintainability. F. Méryd et al. [22] conducted wind tunnel tests on a high-aspect-ratio HLFC wing model with variable-porosity micro-perforated skin in ONERA's S1MA wind tunnel. Combined with numerical simulations, they validated transition prediction methods, evaluated the control effectiveness of variable-porosity suction devices, and analyzed leading-edge attachment-line contamination characteristics. In recent years, with advancements in computational fluid dynamics (CFD), numerical simulations have become the primary research tool for boundary layer suction studies due to their flexible parameter adjustment and comprehensive flow-field information. Researchers have developed integrated numerical frameworks by coupling transition prediction modules with RANS solvers, enabling systematic analysis of how suction location and suction intensity affect transition position and aerodynamic performance.

Optimization design of HLFC typically focuses on two aspects: suction distribution optimization or airfoil shape refinement. Zhao et al. [23] conducted constraint analysis for test-section design of flight-test-oriented HLFC wings, optimized the aerodynamic configuration of wing/pod/pylon assemblies, and comparatively evaluated different suction distributions. Their numerical simulations and wind tunnel tests validated the effectiveness of the optimized configuration in suppressing crossflow (CF) disturbance transition and delaying transition location through suction. They concluded that a compromise suction distribution could balance transition control performance with power-flow constraints. For highly swept three-dimensional wings, leading-edge suction primarily suppresses CF instability. Zhu Zhen [24] demonstrated that, under identical suction intensity, expanding suction coverage further reduces the cumulative amplification factor of crossflow disturbances, thereby delaying transition. Shi et al. [25] optimized HLFC for infinite-swept wings and found that, under fixed lift coefficient constraints, the optimized suction distribution could expand the laminar flow region and reduce total drag. Sudhi et al. [26] explored a transonic HLFC design for infinite-swept wings using a multi-fidelity framework integrated with multi-objective genetic algorithms to simultaneously optimize airfoil geometry and suction distribution. They identified optimal low-drag airfoils and sweep angles under varying design conditions, verifying the drag reduction benefits of HLFC over natural laminar flow (NLF) configurations.

Despite rapid advancements in suction distribution optimization methodologies, systematic parametric studies on suction parameter optimization for HLFC remain limited. Comprehensive comparative analyses of how the suction coefficient, suction location, and suction hole diameter affect transition characteristics and overall aerodynamic performance of two-dimensional airfoils are still lacking. A summary of previous HLFC studies is provided in Table 1 to highlight the research gap. The originality of this study lies in its systematic investigation of parametric optimization for HLFC on two-dimensional airfoils, specifically addressing the gap in comprehensive comparative studies regarding the synergistic effects of suction coefficient (C_q = 5.2 × 10^{-5}~9.6 × 10^{-4}), location (5% c, 10% c, and 15% c, where c denotes the chord length), and suction hole diameter (0.2 mm, 0.6 mm, and 1.0 mm). The primary contributions to the literature are threefold: first, this work establishes quantitative guidelines for parameter matching, demonstrating that an optimal interval exists between the suction location and coefficient, and that smaller suction hole diameters (0.2 mm) yield superior drag reduction efficiency; second, the underlying

mechanisms are differentiated by revealing that the suction location predominantly governs the viscous drag coefficient, whereas the suction hole diameter primarily influences the pressure drag coefficient; third, an energy-saving design strategy is proposed, advocating for the employment of small apertures across the suction region with a gradually increasing suction flow rate toward the trailing edge. These findings provide critical references for the engineering design and optimization of HLFC systems.

Table 1. Summary of previous experimental and numerical studies on HLFC.

Author	Experimental/Numerical Conditions	Key Findings and Mechanisms
Schmitt et al. [17]	A320 Vertical Tail Flight Test	Validated the engineering feasibility of HLFC; maintained a large-scale laminar flow region on the vertical tail surface.
Geng et al. [18]	2D Airfoil, Low-turbulence Wind Tunnel	Demonstrated that proper suction can delay transition from 40% to beyond 80% chord, achieving significant drag reduction.
Wong et al. [19]	Swept Wing Test	Found that standard suction delays transition to 80% chord; double suction maintains laminar flow up to 85% chord, verifying suppression of leading-edge disturbances.
Shi et al. [20]	Transonic Wind Tunnel Test	Calibrated equivalence between discrete-hole and continuous suction; verified RANS-e^N method accuracy (error < 4% chord); analyzed CF vortex suppression.
Scholz et al. [21]	1:0.7 Scale Vertical Tail, DNW-LLF Wind Tunnel	Verified Tailored Skin Single Duct (TSSD) system; solved scalability and maintainability issues of traditional suction systems.
Méry et al. [22]	High Aspect Ratio Wing, ONERA S1MA Tunnel	Validated variable-porosity micro-perforated skin; analyzed leading-edge attachment-line contamination characteristics.
This Study	NACA66012 and Target Airfoil, Numerical Simulation	1. Parameter matching: identified optimal interval between location/coefficients; 2. Mechanism differentiation: location governs viscous drag, diameter governs pressure drag; 3. Design strategy: proposed small apertures with increasing suction rate toward trailing edge.

2. Materials and Methods

2.1. γ-$\widetilde{Re}_{\theta t}$ Transition Model

The correlation-based γ-$\widetilde{Re}_{\theta t}$ transition model [27] is formulated exclusively with local variables, ensuring robust compatibility with contemporary computational fluid dynamics (CFD) frameworks. By correlating $\widetilde{Re}_{\theta t}$ directly with local strain rate maxima (which exhibit strong dependence on vorticity in critical flow regions), the model obviates traditional momentum thickness calculations. Furthermore, the implementation of a $\widetilde{Re}_{\theta t}$ transport equation also precludes reliance on non-local empirical correlations, thereby streamlining computational procedures. The intermittency transport equation (Equation (1)) incorporates wall-sensitive source terms, enabling direct capture of suction-induced modifications to boundary layer velocity profiles and transition onset delays. Consequently, the model demonstrates exceptional suitability for HLFC simulations. It comprises two transport equations, specifically designed to characterize intermittency and the momentum thickness Reynolds number, respectively.

The transport equation for the intermittency factor γ is defined as:

$$\frac{\partial(\rho\gamma)}{\partial t} + \frac{\partial(\rho U_j\gamma)}{\partial x_j} = P_{\gamma 1} - E_{\gamma 1} + P_{\gamma 2} - E_{\gamma 2} + \frac{\partial}{\partial x_j}\left[\left(\mu + \frac{\mu_t}{\sigma_\gamma}\right)\frac{\partial\gamma}{\partial x_j}\right] \tag{1}$$

The transition source term is defined as follows:

$$P_{\gamma 1} = C_{\alpha 1} F_{length} \rho S [\gamma F_{onset}]^{C_{\gamma 3}} \tag{2}$$

$$E_{\gamma 1} = C_{e1} P_{\gamma 1} \gamma \tag{3}$$

where S denotes the magnitude of the strain rate, F_{length} represents the length of the transition region, and $C_{\alpha 1} = 2$, $C_{e1} = 1$ are constants. The destruction term/relaminarization term is defined as follows:

$$P_{\gamma 2} = C_{\alpha 2} \rho \Omega \gamma F_{turb} \tag{4}$$

$$E_{\gamma 2} = C_{e2} P_{\gamma 2} \gamma \tag{5}$$

where Ω denotes the magnitude of the vorticity. The onset of transition is controlled by the following equation:

$$Re_V = \frac{\rho y^2 S}{\mu} \tag{6}$$

$$R_T = \frac{\rho k}{\mu \omega} \tag{7}$$

$$F_{onset1} = \frac{Re_v}{2193 Re_{\theta c}} \tag{8}$$

$$F_{onset2} = \min\left(\max\left(F_{onset1}, F_{onset1}^4\right), 2.0\right) \tag{9}$$

$$F_{onset3} = \max\left(1 - \left(\frac{R_T}{25}\right)^3, 0\right) \tag{10}$$

$$F_{onset} = \max(F_{onset2} - F_{onset3}, 0) \tag{11}$$

$$F_{turb} = e^{\left(\frac{R_T}{4}\right)^4} \tag{12}$$

where γ denotes the intermittency factor (not the distance to the wall; see the correction note below), and $Re_{\theta c}$ represents the critical momentum thickness Reynolds number at which the intermittency function begins to increase within the boundary layer.

The constant values for the intermittency factor equation are specified as follows:

$$C_{\alpha 1} = 2; C_{e1} = 1; C_{\alpha 2} = 0.06; C_{e2} = 50; C_{\gamma 3} = 0.5; \sigma_\gamma = 1.0$$

The transport equation for the transition momentum thickness Reynolds number ($\widetilde{Re}_{\theta t}$) is:

$$\frac{\partial\left(\rho\widetilde{Re}_{\theta t}\right)}{\partial t} + \frac{\partial\left(\rho U_j \widetilde{Re}_{\theta t}\right)}{\partial x_j} = P_{\theta t} + \frac{\partial}{\partial x_j}\left[\sigma_{\theta t}(\mu + \mu_t)\frac{\widetilde{Re}_{\theta t}}{\partial x_j}\right] \tag{13}$$

The source terms are defined as follows:

$$P_{\theta t} = C_{\theta t}\frac{\rho}{t}\left(Re_{\theta t} - \widetilde{Re}_{\theta t}\right)(1.0 - F_{\theta t}) \tag{14}$$

$$t = \frac{500\mu}{\rho U^2} \tag{15}$$

$$F_{\theta t} = \min\left(\max\left(F_{wake}e^{\left(\frac{y}{\delta}\right)^4}, 1.0 - \left(\frac{\gamma - 1/50}{1.0 - 1/50}\right)^2\right), 1.0\right) \tag{16}$$

$$\theta_{BL} = \frac{\widetilde{Re}_{\theta t}\mu}{\rho U} \tag{17}$$

$$\delta_{BL} = \frac{15}{2}\theta_{BL} \tag{18}$$

$$\delta = \frac{50\Omega y}{U}\delta_{BL} \tag{19}$$

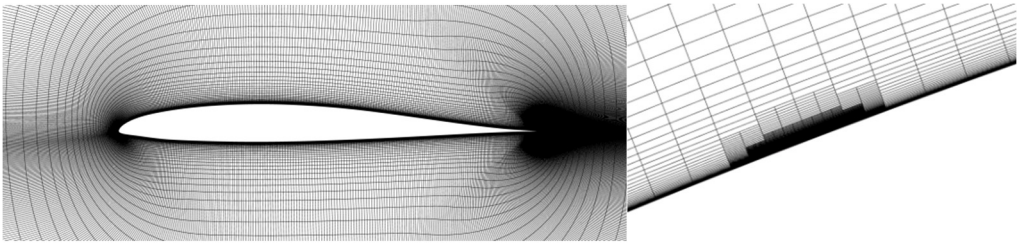
$$Re_{\omega} = \frac{\rho\omega y^2}{\mu} \tag{20}$$

$$F_{wake} = e^{-\left(\frac{Re_{\omega}}{1E+5}\right)^2} \tag{21}$$

The values of the associated constants are as follows: $C_{\theta t} = 0.03; \sigma_{\theta t} = 2.0$.

2.2. Physical Model and Solution Method

In this paper, a custom-designed airfoil with a chord length of 0.1 m and tailored geometry optimized for laminar flow control is investigated. To accurately resolve the boundary layer flow, the first-layer grid height at the wall satisfies y^+ = 0.2–1. The total computational grid size comprises approximately 150,000 nodes, with the grid arrangement around the airfoil depicted in Figure 2. Single suction holes are positioned at 5%, 10%, and 15% chord lengths along the chordwise direction of the airfoil. Given that the suction hole diameter is significantly smaller than the airfoil chord length, local grid refinement is applied in the vicinity of the suction holes to maintain computational accuracy while controlling grid scale and conserving computational resources. The computational domain boundaries are uniformly set at 150 chord lengths from the airfoil surface.



(**a**) (**b**)

Figure 2. Computational domain mesh: (**a**) grid distribution around the airfoil; (**b**) enlarged view of the suction hole.

This study is based on the assumption of steady compressible flow. The governing equations solved comprise the mass-weighted Navier–Stokes (N-S) equations, energy equation, and γ-$\widetilde{Re}_{\theta t}$ transition model. Computations employ a double-precision solver, with the governing equations discretized via the finite volume method. Convective terms are discretized using a second-order upwind scheme, while diffusive terms adopt a central differencing scheme. Pressure-velocity coupling is resolved using the Coupled algorithm. A no-slip boundary condition is applied at the airfoil surface, and pressure far-field boundary conditions are imposed for regions sufficiently distant from the airfoil surface.

2.3. Validation Cases

To verify the reliability of the numerical methodology, this study adopts the NACA66012 airfoil wind tunnel experiment conducted by Wright and Nelson [28] as the benchmark. The experiment was performed in the low-speed wind tunnel at the Uni-

versity of Southampton (UK), with a freestream velocity of 20 m/s, turbulence intensity of approximately 0.1%, and a model mounting angle of attack of −1°. The test model is based on a NACA 66012 airfoil with an original chord length of 1 m, but a 1-m-long flat plate section is inserted at its maximum thickness position, resulting in a total chord length of 2 m for the test model (as shown in Figure 3). The suction region spanned 23–42% chordwise and was equipped with a micro-hole array of 0.1 mm diameter (width) and 1 mm pitch. The transition detection system employed an array of miniature electret microphones. These microphones were mounted behind 0.5 mm diameter holes on the surface. The signals were high-pass filtered at 800 Hz to remove tunnel noise and low-frequency components. The root mean square (RMS) of the pressure fluctuations was then calculated to distinguish between laminar and turbulent boundary layers.

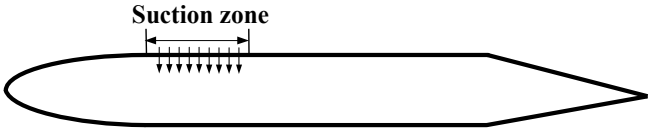


Figure 3. Suction control diagram of NACA66012 airfoil.

To assess the applicability of the γ-$\widetilde{Re}_{\theta t}$ transition model for suction-based flow control, this study conducted multi-case numerical simulations on the NACA66012 airfoil and compared results with experimental data. As shown in Table 2, the computed transition location displacement x_{tr} (defined as the streamwise distance from the suction region exit to the transition onset point) at various dimensionless suction coefficients (C_q) exhibits agreement with measurements (mean error = −2.71%). This confirms the model's capability to reliably capture the transition delay effect induced by suction.

Table 2. Comparison of calculated and experimental aerodynamic characteristics for the experimental model.

Suction Coefficient ($C_q \times 10^{-4}$)	Experimental Value Δx_{tr}/(m)	Calculated Value Δx_{tr}/(m)	Relative Error
0.00	0.0201	0.0186	−7.46%
0.30	0.0792	0.0759	−4.22%
0.65	0.1773	0.1905	7.45%
0.97	0.2892	0.2913	0.73%
1.35	0.3806	0.3910	2.74%
1.65	0.4661	0.4517	−3.09%
1.85	0.5225	0.4880	−6.59%
2.00	0.5545	0.5181	−6.58%
2.18	0.5739	0.5316	−7.38%

Experimental data were digitized from the figure [28].

The coefficients of lift and pressure were not validated owing to the absence of comparable data in ref. [28]. The calculated drag coefficient was compared with experimental data, as shown in Table 3. The comparison results (mean error = 3.24%) validate the accuracy of the numerical simulation methodology employed in this study.

Table 3. Comparison of calculated and experimental aerodynamic characteristics (C_D) for the experimental model.

AOA	Suction Coefficient ($C_q \times 10^{-4}$)	C_D		
		Experimental Value	Calculated Value	Relative Error
−1°	0.00	0.2650	0.2894	9.21%
−1°	0.30	0.2625	0.2771	5.56%
−1°	0.65	0.2612	0.2404	−7.97%
−1°	0.97	0.2597	0.2542	−2.12%
−1°	1.35	0.2573	0.2479	−3.63%
−1°	1.65	0.2566	0.2669	4.04%
−1°	1.85	0.2563	0.2762	7.76%
−1°	2.00	0.2557	0.2750	7.55%
−1°	2.18	0.2541	0.2763	8.74%

Experimental data were digitized from the figure [28].

2.4. Suction Parameters

Before analyzing the computational results, a dimensionless suction coefficient is first defined, which represents the mass flow rate per unit time. The expression is as follows:

$$C_q = \frac{Q}{bcU_\infty \rho_\infty} \tag{22}$$

In the equation, Q denotes the mass flow rate of air inhaled through the suction holes per unit time; b is the spanwise length; c is the chord length. For a two-dimensional airfoil, $Q = \rho_s v_s n d$, where ρ_s is the suction air density with $\rho_s = \rho_\infty$, v_s is the suction velocity, n is the number of suction holes, d is the width of each suction hole, and $b = 1$ (unit span). Consequently, Equation (22) can be written as follows:

$$C_q = \frac{n d v_s}{c U_\infty} \tag{23}$$

3. Results

3.1. Transition Characteristics of the Pristine Airfoil Under Suction-Free Conditions

In this study, the transition position on the airfoil surface is determined according to the abrupt change point of the skin friction coefficient (C_f). This study extrapolates the transition prediction methodology validated for the NACA66012 airfoil to a target airfoil to assess its aerodynamic characteristics and the effects of suction-based flow control on the transition region. Figure 4 presents the C_f distribution under suction-free conditions at the design point, defined by a chord-based Reynolds number $Re = 8 \times 10^6$ ($c = 0.1$ m), Mach number $Ma = 0.5$, freestream turbulence intensity $Tu = 0.3\%$, lift coefficient $C_L = 0.18$, and reference static pressure $p_{ref} = 1.68 \times 10^5$ Pa. Numerical simulations were conducted at a fixed angle of attack $\alpha = 0°$, with the transition onset point on the upper surface predicted at $x_{tr} = 23.21\%c$ measured from the leading edge.

3.2. Effects of Boundary Layer Suction Parameters on Transition Delay

3.2.1. Influence of the Suction Coefficient

First, suction hole diameters of 0.2 mm, 0.6 mm, and 1.0 mm were selected, with suction locations positioned at the 5% chord, 10% chord, and 15% chord. For each combination of hole diameter and location, the laminar–turbulent transition position on the airfoil was computed across varying suction coefficients. Figure 5 presents the surface skin friction

coefficient distributions along the upper airfoil surface under different suction coefficients. Here, $C_q = 0$ signifies the baseline case without suction control.

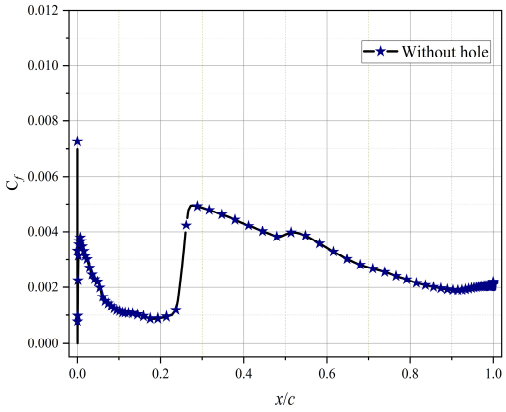


Figure 4. Airfoil skin friction coefficient distribution: x-axis: normalized streamwise position (x/c); y-axis: skin friction coefficient (C_f).

As observed in the figure, at a fixed Reynolds number, suction delays the onset of boundary layer transition on the upper surface relative to the uncontrolled case. With an increasing suction coefficient (C_q), the transition point progressively shifts toward the trailing edge. Concurrently, suction elevates the laminar-region skin friction coefficient within the suction zone. This arises because suction thins the boundary layer and intensifies wall shear stress. This phenomenon is further corroborated by the analytical expression for surface skin friction coefficient derived from the suction-modified momentum integral equation [29].

$$C_f = \frac{\tau_w}{\frac{1}{2}\rho_\infty u_\infty^2} = 2\frac{d\delta_2}{dx} - 2\frac{\rho_w sgn(v_w)|v_w|}{\rho_\infty u_\infty} + 2\delta_2\left[\frac{1}{\rho_\infty}\bullet\frac{d\rho_\infty}{dx} + \frac{1}{u_\infty}\left[2+\frac{\delta_1}{\delta_2}\right]\frac{du_\infty}{dx} + \frac{1}{R}\bullet\frac{dR}{dx}\right] \quad (24)$$

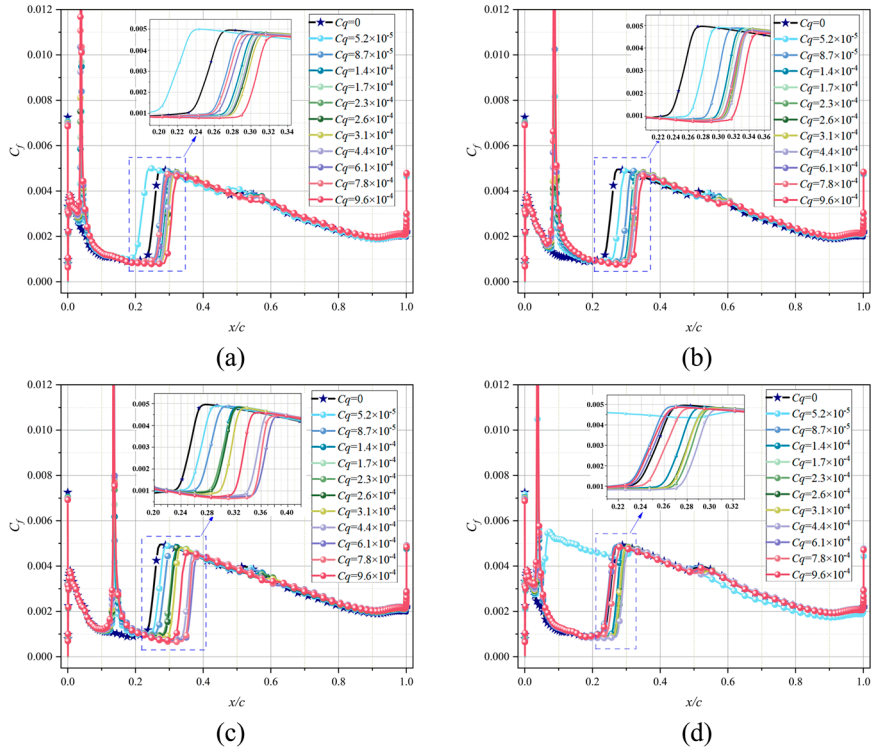


Figure 5. *Cont.*

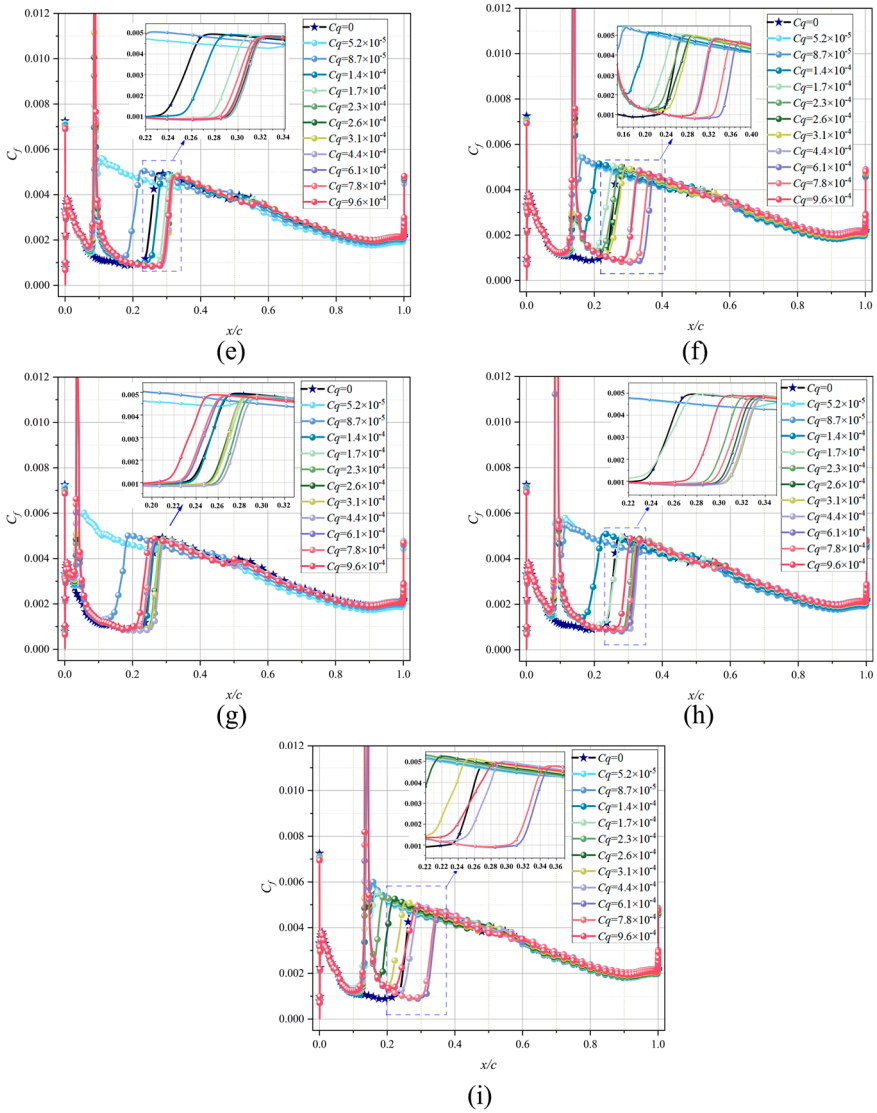


Figure 5. Variation plot of laminar–turbulent transition location on the upper airfoil surface with suction coefficient for three suction locations (5%, 10%, and 15% chord) and three suction hole diameters (0.2 mm, 0.6 mm, and 1.0 mm): (**a**) x_{hole} = 5% c, d = 0.2 mm; (**b**) x_{hole} = 10% c, d = 0.2 mm; (**c**) x_{hole} = 15% c, d = 0.2 mm; (**d**) x_{hole} = 5% c, d = 0.6 mm; (**e**) x_{hole} = 10% c, d = 0.6 mm; (**f**) x_{hole} = 15% c, d = 0.6 mm; (**g**) x_{hole} = 5% c, d = 1 mm; (**h**) x_{hole} = 10% c, d = 1 mm; (**i**) x_{hole} = 15% c, d = 1 mm; x-axis: normalized streamwise position (x/c); y-axis: skin friction coefficient (Cf).

In the equation, variables with subscript w denote physical quantities at the wall; R is the radius of curvature of the aerodynamic surface; δ_1 is the boundary layer displacement thickness; δ_2 is the boundary layer momentum thickness; v_w is the flow velocity normal to the airfoil surface. The sign function can be written as:

$$sgn(v_w) = \begin{cases} -1 & v_w < 0,\ suction \\ 0 & v_w = 0 \\ 1 & v_w > 0,\ blow \end{cases} \tag{25}$$

From Equation (25), it follows that suction applied to the wall renders the second term on the right-hand side of Equation (24) positive, thereby increasing the skin friction coefficient. Conversely, blowing reduces the skin friction coefficient.

It can be observed from Figure 5 that insufficient suction causes premature transition. The minimum C_q values achieving drag reduction under all operating conditions in Figure 5 are summarized in Table 4. It is also evident that under mild suction conditions, the transition location progressively shifts downstream as the suction coefficient increases; within a certain range, further increasing the suction coefficient gradually moves the transition location toward the trailing edge, yet the growth rate of the laminar region progressively decelerates and eventually asymptotically approaches a fixed position. Moreover, larger suction coefficients entail higher energy consumption, while the growth of the laminar region increasingly plateaus, indicating that the efficiency of laminar flow control fundamentally deteriorates. Therefore, for a single suction hole, employing substantially larger suction coefficients beyond this asymptotic point constitutes energy inefficiency in delaying transition. Figure 6 provides a contour plot of the laminar–turbulent transition location on the upper airfoil surface versus the suction coefficient for the 15% chord suction location with a 0.2 mm suction hole diameter. The delay in transition with increasing suction coefficient can be attributed to the stabilization of the boundary layer velocity profile. Suction removes low-momentum fluid from the near-wall region, which increases the shape factor of the boundary layer. This modified velocity profile is more stable against the growth of Tollmien–Schlichting (T-S) waves, thereby suppressing the breakdown to turbulence.

Table 4. Minimum C_q values achieving drag reduction across operating conditions (Figure 5).

x_{hole}	d/(mm)	Min C_q for Drag Reduction
5% *c*	0.2	8.7×10^{-5}
10% *c*	0.2	5.2×10^{-5}
15% *c*	0.2	5.2×10^{-5}
5% *c*	0.6	1.4×10^{-4}
10% *c*	0.6	1.4×10^{-4}
15% *c*	0.6	2.6×10^{-4}
5% *c*	1.0	1.4×10^{-4}
10% *c*	1.0	2.3×10^{-4}
15% *c*	1.0	4.4×10^{-4}

3.2.2. Effect of Suction Location

Figure 7 presents the relationship between the suction coefficient and laminar–turbulent transition location on the upper airfoil surface for different suction locations. It can be observed that under mild suction conditions, as the suction hole location moves progressively rearward, the slope of the relationship between suction coefficient and transition location on the upper airfoil surface gradually decreases, indicating that the more forward the suction hole location, the more sensitive the transition location is to changes in suction coefficient. At the 5% chord location, as the hole diameter increases, the range of suction coefficients producing effective transition delay progressively narrows, or equivalently, the minimum suction coefficient required for observable transition delay gradually increases. It is also evident that among the three hole diameters, the smallest diameter (d = 0.2 mm) achieves the optimal transition delay effect at identical suction coefficients; furthermore, at the 15% chord location with larger suction coefficients, the most effective transition delay is attained, advancing the transition location to 35.01% chord, which represents a delay of 11.8% chord relative to the original transition location (23.21% chord). For a large diameter (d = 1 mm), a small C_q value suffices for drag reduction when the position is forward (5% *c*), whereas a larger C_q value is required when the position is rearward (15% *c*).

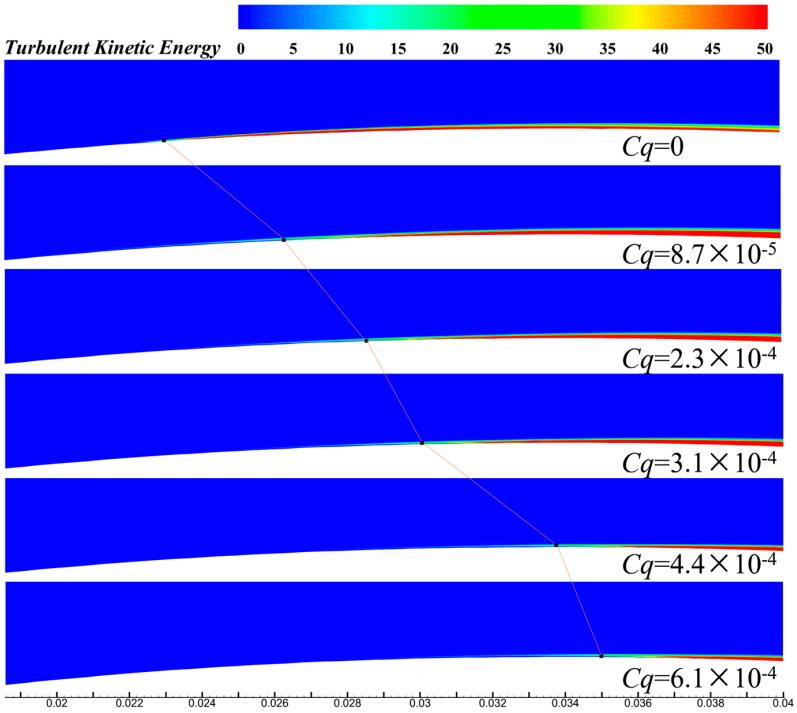


Figure 6. Variation plot of laminar–turbulent transition location on the upper airfoil surface with suction coefficient for the 15% chord suction location and 0.2 mm suction hole diameter; x-axis: the streamwise spatial coordinates (in meters) of the airfoil flow field; y-axis: the wall-normal spatial coordinates (in meters) of the airfoil flow field.

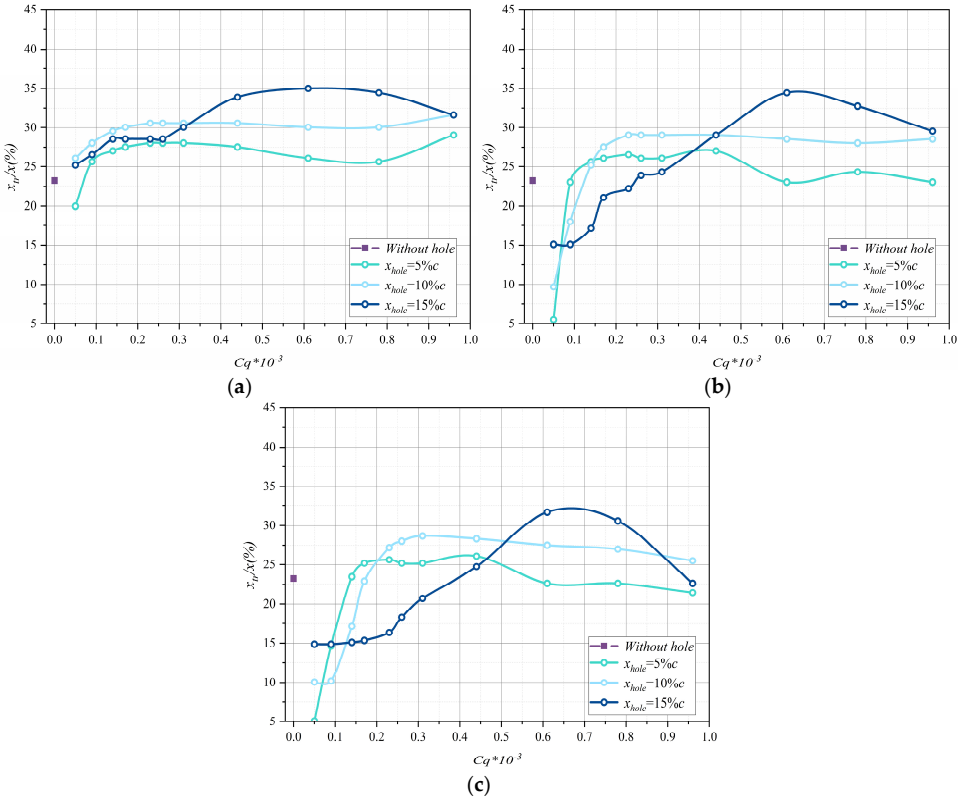


Figure 7. Variation plot of laminar-turbulent transition location on the airfoil upper surface with suction coefficient for identical hole diameters (0.2 mm, 0.6 mm, 1 mm) at different suction locations: (**a**) d = 0.2 mm; (**b**) d = 0.6 mm; (**c**) d = 1 mm; x-axis: dimensionless mass flow coefficient (C_q); y-axis: normalized streamwise transition location.

3.2.3. Effect of Suction Hole Diameter

Figure 8 presents the relationship between suction coefficient and laminar–turbulent transition location on the upper airfoil surface for different suction hole diameters at identical suction locations. It can be observed that among the three suction locations, the smallest hole diameter (d = 0.2 mm) consistently achieves the most effective transition delay. The superior performance of smaller suction holes (d = 0.2 mm) is primarily due to the reduction in discrete suction effects. Smaller holes generate a more uniform suction velocity distribution across the surface, minimizing local flow distortions. In contrast, larger suction holes act as discrete sinks, creating localized strong velocity gradients and potential flow instabilities around the hole edges. These discrete disturbances can trigger premature transition even if the total suction mass flow rate is the same, explaining why smaller diameters yield better transition control efficiency. Comparing Figure 8a–c, the optimal transition delay effect gradually increases while the minimum suction coefficient required for achieving this optimal effect also progressively rises. At the 5% chord location, the smallest hole diameter exhibits superior transition delay performance at identical suction coefficients, yet the range of suction coefficients yielding stable transition delay is relatively narrow. Additionally, pronounced fluctuations are evident over a broader range of higher suction coefficients, indicating unstable suction effectiveness under these conditions. At the 10% chord location, all three holes diameters achieve relatively maximum transition locations at relatively low suction coefficients, followed by a wide range of suction coefficients maintaining stable transition positions. At the rearward position (15%c), the relative maximum transition location for all three aperture sizes is attained at larger C_q values. Furthermore, as the suction coefficient increases beyond this point, the transition location rapidly moves forward, and the range of suction coefficients yielding stable transition delay becomes notably narrower.

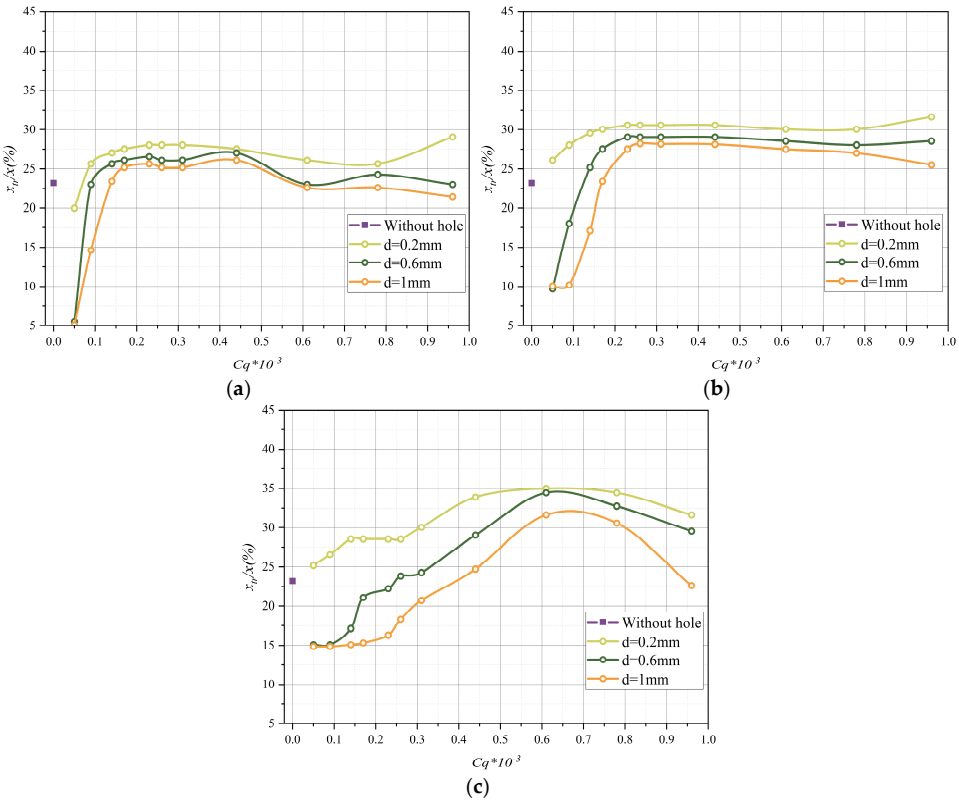


Figure 8. Variation in transition location with suction coefficient for different suction hole diameters at identical suction locations (5%, 10%, and 15% chord): (**a**) x_{hole} = 5%c; (**b**) x_{hole} = 10%c; (**c**) x_{hole} = 15%c; x-axis: dimensionless mass flow coefficient (C_q); y-axis: normalized streamwise transition location.

3.3. Effect of Boundary Layer Suction Parameters on Airfoil Drag

3.3.1. Effect of Suction Coefficient

At the same Reynolds number, when the suction coefficient reaches a specific value where the C_D equals that without suction control ($C_{D\text{-without}}$), i.e., when the reduction in turbulent drag coefficient balances the increase in laminar drag coefficient, the corresponding suction coefficient is defined as the critical suction coefficient. As shown in Figure 9, within a certain range (for example, in the $C_{D\text{-}5\%c}$ condition under (a), the range of C_q is 5.2×10^{-5} ~7×10^{-4}), the C_D first decreases and then increases with an increasing suction coefficient. Specifically, the C_{Dv} initially decreases and subsequently increases, a phenomenon arising from the competitive relationship between the laminar flow extension effect and the turbulent triggering effect, which exhibits an inverse trend as the suction coefficient increases. Meanwhile, the C_{Dp} first decreases and then stabilizes, attributable to the alteration of surface pressure distribution in the suction region and its upstream area induced by suction.

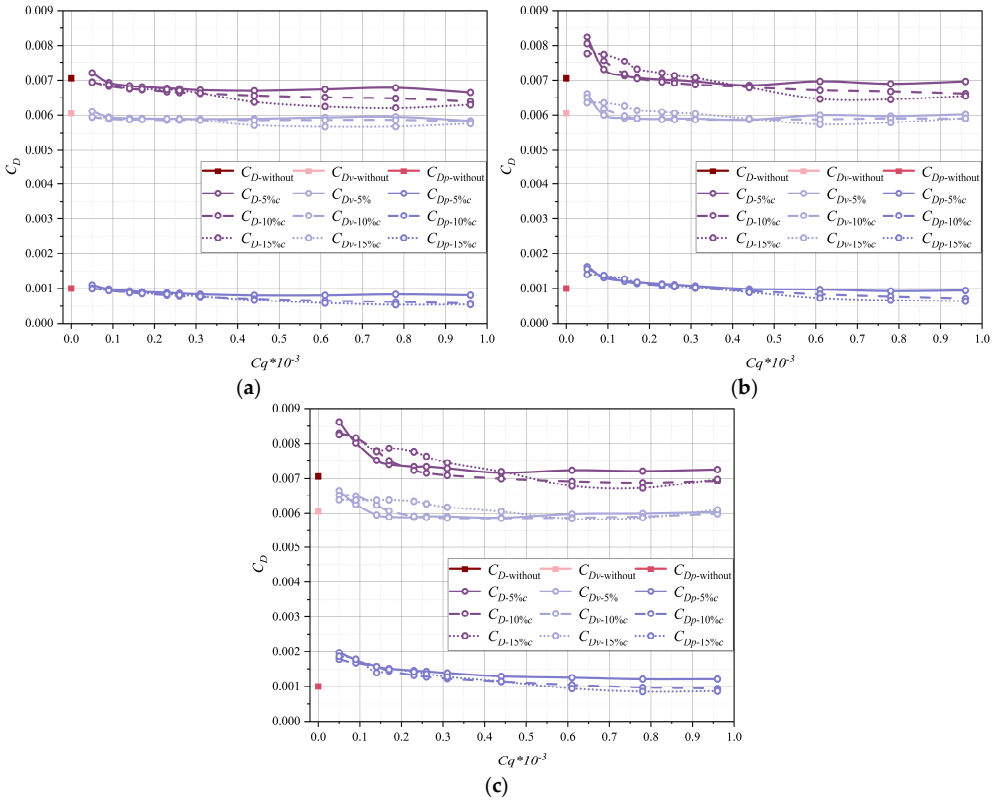


Figure 9. C_D, C_{Dv}, and C_{Dp} versus suction coefficient at different suction locations for identical suction hole diameters (0.2 mm, 0.6 mm, 1 mm): (**a**) d = 0.2 mm; (**b**) d = 0.6 mm; (**c**) d = 1 mm; x-axis: dimensionless mass flow coefficient (C_q); y-axis: drag coefficient.

It can also be observed that, in terms of the drag reduction effect, an optimal matching interval exists between suction location and suction coefficient (Figure 9c); the suction hole diameter influences the size of this interval, with smaller diameters making the interval wider. Under identical hole diameters, drag reduction is relatively more effective when suction is applied at the 5% c location for low suction coefficients, at the 10% c location for moderate suction coefficients, and at the 15% c location for high suction coefficients. At a small hole diameter (d = 0.2 mm) with a substantial suction volume at the 15% c location, the C_D reaches its minimum value of 0.00622 (original drag coefficient: 0.00706), representing an 11.9% reduction. It is evident that the control condition achieving the maximum delay in transition location corresponds to the state with the minimum C_D.

3.3.2. Effect of Suction Location

As shown in Figure 9, the suction location primarily influences the C_D by affecting the C_{Dv}, and it can also be observed that, across the three hole diameters, the differences in C_{Dv} between various suction locations constitute the main factor contributing to variations in the C_D. It also determines the rate of decrease for the three drag coefficients, the minimum suction coefficient required to achieve optimal control effect, and the magnitude of the stabilization plateau.

Figure 10 presents the flow-field diagram for the case with d = 0.6 mm, x_{hole} = 5% c, and C_q= 5.2 × 10^{-5}, demonstrating that an excessively small suction system causes premature transition to occur at the suction hole location (5% c). This is because the insufficient suction flow rate results in inadequate active control capability over the main flow, failing to counterbalance the negative effects, such as the roughness introduced by the suction hole itself and the disturbances generated by the suction. Consequently, the suction system does not achieve the expected flow stabilization effect but instead induces premature transition due to alterations in the flow structure.

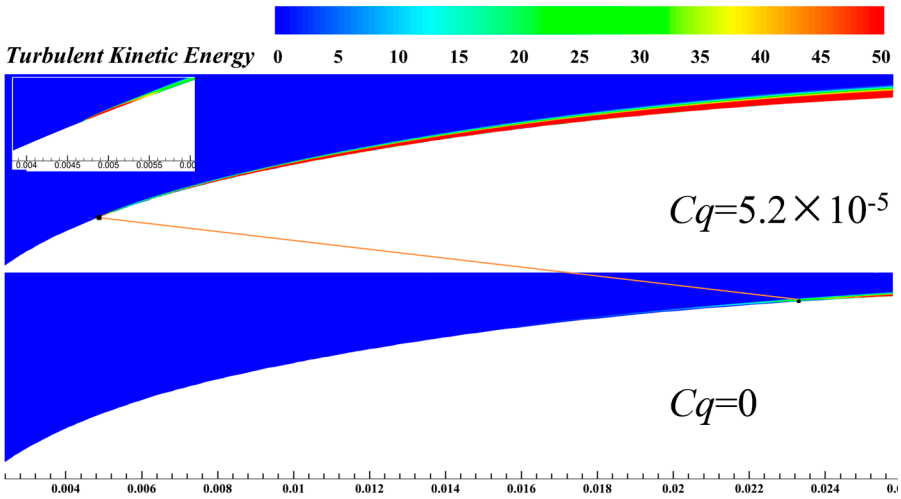


Figure 10. Flow field distribution at d = 0.6 mm, x_{hole} = 5% c, C_q = 5.2 × 10^{-5}; x-axis: the streamwise spatial coordinates (in meters) of the airfoil flow field; y-axis: the wall-normal spatial coordinates (in meters) of the airfoil flow field.

Table 5 presents a summary of the C_D values and C_q ranges corresponding to the optimal drag reduction for each case. It can be observed that, for the three hole diameters, the optimal drag reduction effect achieved by suction control at the 15%c location is superior to that at the 10%c and 5%c locations; it can also be observed that the later the suction location (ahead of the original transition location), the better the achievable optimal drag reduction effect [For d = 0.2 mm, 0.00622 < 0.00640 < 0.00665; for d = 0.6 mm, 0.00646 < 0.00662 < 0.00686; and for d = 1 mm, 0.00673 < 0.00688 < (minimum: 0.00716)], but the larger the minimum suction coefficient required (For d = 0.2 mm, 6.1 × 10^{-4} > 4.1 × 10^{-4} > 2.5 × 10^{-4}; for d = 0.6 mm, 6.1 × 10^{-4} > 5.2 × 10^{-4} > 3.1 × 10^{-4}; and for d = 1 mm, 6.1 × 10^{-4} > 5.5 × 10^{-4} > 3.2 × 10^{-4}). The enhanced effectiveness of aft suction locations is linked to the local Reynolds number (Re_x) effect. As the chordwise position increases, so does Re_x, making the boundary layer more susceptible to instability growth. Applying suction in these high-Re_x regions effectively interrupts the rapid amplification of disturbances. Furthermore, placing the suction slot aft allows for a longer natural laminar flow region upstream, maximizing the net drag reduction benefit while minimizing the energy expenditure on suction.

Table 5. Summary of C_D values and C_q ranges corresponds to the optimal drag reduction for each case (Figure 9).

x_{hole}	d/(mm)	Optimal Drag Reduction	
		C_D	C_q
5% *c*	0.2	0.00665	2.5×10^{-4}~$\underline{9.6 \times 10^{-4}}$
10% *c*	0.2	0.00640	4.1×10^{-4}~$\underline{9.6 \times 10^{-4}}$
15% *c*	0.2	0.00622	6.1×10^{-4}~$\underline{7.8 \times 10^{-4}}$
5% *c*	0.6	0.00686	3.1×10^{-4}~$\underline{4.4 \times 10^{-4}}$
10% *c*	0.6	0.00662	5.2×10^{-4}~$\underline{9.6 \times 10^{-4}}$
15% *c*	0.6	0.00646	6.1×10^{-4}~$\underline{7.8 \times 10^{-4}}$
5% *c*	1.0	-(min: 0.00716)	-(min: 3.2×10^{-4}~$\underline{4.4 \times 10^{-4}}$)
10% *c*	1.0	0.00688	5.5×10^{-4}~$\underline{7.8 \times 10^{-4}}$
15% *c*	1.0	0.00673	6.1×10^{-4}~$\underline{7.8 \times 10^{-4}}$

In the C_q ranges, underlined numbers denote calculated values, whereas non-underlined ones are obtained from the figures.

Under low suction conditions, for suction locations further forward, as the suction coefficient increases, the C_D, C_{Dv}, and C_{Dp} exhibit a faster decreasing trend, quickly reaching a stable plateau region with a longer duration; for suction locations further backward, as the suction coefficient increases, the drag coefficients decrease more slowly, only reaching the stable plateau region for the C_D at higher suction coefficients, with a shorter plateau duration.

It can be observed that as the suction coefficient increases, the differences in C_{Dp} among the three suction locations become larger; therefore, under identical hole diameters, the C_{Dp} becomes increasingly sensitive to suction location with an increasing suction coefficient.

3.3.3. Effect of Suction Hole Diameter

As shown in Figure 11, the suction hole diameter primarily affects the C_D by influencing the C_{Dp}. It can also be observed that, at the three locations, the differences in C_{Dp} among different hole diameters are the main factors affecting the variations in C_D; therefore, the suction hole diameter has a significant impact on the C_{Dp}. At the three locations, a smaller hole diameter results in lower C_D, C_{Dv}, and C_{Dp} under the same suction coefficient, yielding a better drag reduction effect.

When the suction location is forward (Figure 11a), only smaller hole diameters (d = 0.2 mm, 0.6 mm) exhibit drag reduction effects, and the drag reduction effect is relatively weak; as the suction location moves rearward (Figure 11b,c), the hole diameters that produce drag reduction effects also increase (d = 1 mm); and as the suction location moves rearward, the drag reduction effects for all hole diameters gradually increase, but the hole diameter with the optimal drag reduction effect remains smallest (d = 0.2 mm). For large hole diameters (d = 1 mm), when the suction location is forward (x/c = 5%) and laminar flow control is applied, regardless of the suction coefficient, it results in the C_D of the airfoil being greater than that without suction. Therefore, it is concluded that to achieve drag reduction effects with large hole diameters, it is only possible when placed at a more rearward position (ahead of the original transition location).

By comparing Figure 11a–c, it can be observed that as the suction hole diameter decreases, the minimum suction coefficient required to achieve a drag reduction effect at the same suction location gradually reduces, while the optimal drag reduction effect progressively enhances. Therefore, a smaller hole diameter yields a better drag reduction performance under suction control.

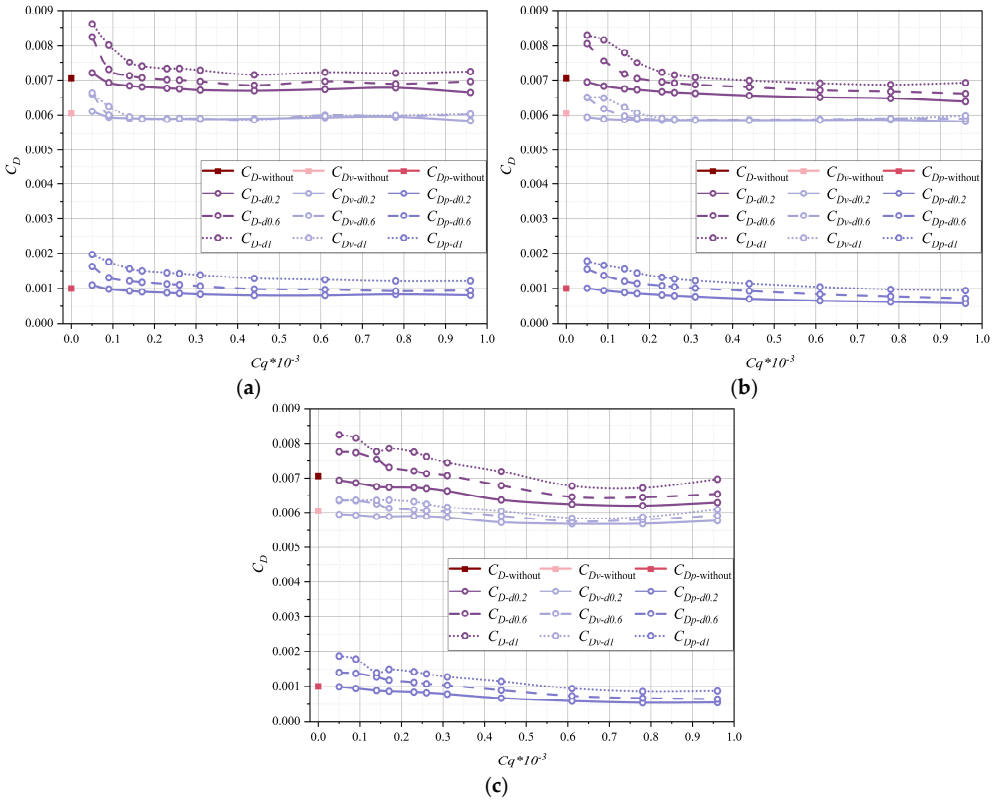


Figure 11. At the same positions (5% *c*, 10% *c*, 15% *c*), variations in C_{Dp} and C_{Dv} with suction coefficients for different suction hole diameters: (**a**) x_{hole} = 5% *c*; (**b**) x_{hole} = 10% *c*; (**c**) x_{hole} = 15% *c*; x-axis: dimensionless mass flow coefficient (C_q); y-axis: drag coefficient.

4. Conclusions

Despite the widespread application of HLFC in modern aerospace engineering, there remains a significant gap in the literature regarding the systematic parametric optimization of suction parameters for two-dimensional airfoils. This study bridges this gap by conducting a detailed numerical investigation using the validated γ-$\widetilde{Re}_{\theta t}$ transition model. Based on the simulation results of the target airfoil, the following quantitative conclusions are drawn:

1. Optimal Drag Reduction Performance: This study identifies that maximum drag reduction is achieved under specific parametric combinations. Specifically, utilizing a small suction hole diameter (d = 0.2 mm) with a relatively high suction coefficient ($C_q \approx 6.1 \times 10^{-4}$) at the aftmost position (5% *c*) yields the minimum drag coefficient (C_D = 0.00622). This represents an 11.9% reduction compared to the baseline (non-suction) case (C_D = 0.00706). Concurrently, this configuration achieves the maximum transition delay, shifting the transition location from 23.21% *c* to 35.01% *c* (a downstream shift of 11.8% chord length).

2. Mechanism Differentiation: The analysis reveals distinct physical mechanisms governing the influence of geometry and parameters. The suction location primarily affects the C_{Dv}, whereas the suction hole diameter predominantly influences the C_{Dp}. Quantitatively, C_{Dv} accounts for the larger proportion of the total drag, indicating that the selection of suction location is more critical for drag reduction than the selection of suction hole diameter.

3. Parametric Sensitivity: The results demonstrate a clear size effect regarding suction hole diameter. The minimum suction coefficient required to achieve drag reduction is indirectly proportional to the hole diameter. Specifically, the threshold C_q for d = 0.2 mm (2.5×10^{-4}) is significantly lower than that for d = 1.0 mm (3.2×10^{-4}). Furthermore,

the optimal matching interval between suction location and coefficient is widest for small diameters and widens with increasing hole size.

4. Design Strategy: Based on quantitative analysis, the most energy-efficient strategy for HLFC system design is to employ small suction holes ($d \leq 0.2$ mm) across the entire suction region and gradually increase the suction flow rate as the location moves aft (towards 15% c). This strategy maximizes the laminar flow extension effect while minimizing the energy penalty associated with excessive suction.

This study provides a reference for the design and optimization of suction parameters in airfoil hybrid laminar flow control. Looking ahead, our research team plans to further explore the synergistic application of HLFC with active flow control technologies (e.g., synthetic jets, combined blowing and suction control, etc.) based on existing HLFC advancements, aiming to expand HLFC's applicability in complex flow scenarios such as high-angle-of-attack conditions and provide new insights for aerodynamic optimization of aircraft under multi-operational conditions.

Author Contributions: Conceptualization, D.L. (Dawei Liu) and Y.T.; methodology, D.L. (Daxin Liao); software, C.Z. and H.W.; validation, S.G., G.L., and X.K.; formal analysis, C.Z.; investigation, C.Z.; resources, Y.T.; data curation, D.L. (Daxin Liao); writing—original draft preparation, C.Z.; writing—review and editing, Y.T.; visualization, H.W.; supervision, H.W.; project administration, Y.T.; funding acquisition, Y.T. All authors have read and agreed to the published version of the manuscript.

Funding: This research received no external funding.

Data Availability Statement: Data are available on request due to restrictions.

Conflicts of Interest: The authors declare no conflicts of interest. The funders had no role in the design of the study; in the collection, analyses, or interpretation of data; in the writing of the manuscript; or in the decision to publish the results.

Abbreviations

The following abbreviations are used in this manuscript:

HLFC	Hybrid Laminar Flow Control
NLF	Natural Laminar Flow
T-S	Tollmien–Schlichting
CFD	Computational Fluid Dynamics
TSSD	Tailored Skin Single Duct
CF	Cross Flow
RANS	Reynolds-Averaged Navier–Stokes
C_D	Drag Coefficient
C_{Dv}	Viscous Drag Coefficient
C_{Dp}	Pressure Drag Coefficient
C_f	Skin Friction Coefficient

References

1. Jentys, M.; Breitsamter, C. Aerodynamic drag reduction through a hybrid laminar flow control and variable camber coupled wing. *Aerosp. Sci. Technol.* **2023**, *142*, 108652. [CrossRef]
2. Zhang, J.; Zhang, T.; Yuan, J.; Zeng, Y. Design, simulation, and experimental validation of a HLFC system. *J. Phys. Conf. Ser.* **2025**, *3078*, 012048. [CrossRef]
3. Fröhler, B.M.; Pohya, A.A.; Häßy, J.; Kilian, T.; Bismark, A.H.; Radestock, M.; Palacios, D.C. Performance and economic assessment of a wing-integrated hybrid laminar flow control system. *Aeronaut. J.* **2025**, *129*, 2103–2130. [CrossRef]
4. Abbas, A.; de Vicente, J.; Valero, E. Aerodynamic technologies to improve aircraft performance. *Aerosp. Sci. Technol.* **2013**, *28*, 100–132. [CrossRef]

5. European Commission; Directorate General for Research and Innovation. Directorate General for Mobility and Transport. In *Flightpath 2050: Europe's Vision for Aviation: Maintaining Global Leadership and Serving Society's Needs*; Publications Office: Luxembourg, 2011.
6. Wahlich, M.; Bismark, A.; Radestock, M.; Menchel, K.; Milot, M.; Cruz, D. Hybrid laminar flow control activities within the frame of clean sky 2. In Proceedings of the AIAA SCITECH 2024 Forum, Orlando, FL, USA, 8–12 January 2024.
7. Zhu, Z.; Ju, S.; Wu, Z. Active/passive control technology of laminar flow. *Acta Aeronaut. Astronaut. Sin.* **2016**, *37*, 2065–2090. (In Chinese)
8. Prasannakumar, A.; Sudhi, A.; Seitz, A.; Badrya, C. Design of hybrid-laminar-flow-control wing and suction system for transonic midrange aircraft. *J. Aircr.* **2024**, *61*, 709–732. [CrossRef]
9. Lobitz, L.; Traub, H.; Overbeck, M.; Bień, M.; Heimbs, S.; Hühne, C.; Friedrichs, J.; Horst, P. Aircraft wing design for extended hybrid laminar flow control. *Aerospace* **2023**, *10*, 938. [CrossRef]
10. Chen, Y.; Rao, H.; Xiong, N.; Fan, J.; Shi, Y.; Yang, T. Adjoint-based robust optimization design of laminar flow airfoil under flight condition uncertainties. *Aerosp. Sci. Technol.* **2023**, *140*, 108465. [CrossRef]
11. Zhu, Z.; Wu, Z.; Ding, J. Laminar flow control technology and application. *Acta Aeronaut. Astronaut. Sin.* **2011**, *32*, 765–784. (In Chinese)
12. Wang, Y.; Lan, X.; Shi, Y.; Hua, J.; Bai, J.; Zhou, Z. Gradient optimization design of laminar airfoil considering suction effect. *Acta Aeronaut. Astronaut. Sin.* **2022**, *43*, 383–400. (In Chinese)
13. Song, W.; Wu, M.; Zhu, Z.; Wu, T.; Nie, H.; Fan, T.; Han, Z. Study on transition prediction method for laminar drag reduction design. *Acta Aerodyn. Sin.* **2018**, *36*, 213–228. (In Chinese)
14. Yang, T.; Bai, J.; Shi, Y.; Yang, Y.; Lu, L. Optimization design of HLFC wing considering the influence of suction distribution. *Acta Aeronaut. Astronaut. Sin.* **2017**, *38*, 6–20. (In Chinese)
15. Jiang, L.; Rao, H.; Lan, X.; Yang, T.; Geng, J.; Bai, J. Aerodynamic design and comprehensive income impact of mixed laminar wing. *Acta Aeronaut. Astronaut. Sin.* **2022**, *43*, 311–330. (In Chinese)
16. NASA. *High Reynolds Number Hybrid Laminar Flow Control (HLFC) Flight Experiment: Suction System Design and Manufacture—Report 4*; NASA: Washington, DC, USA, 1999.
17. Schmitt, V.; Archambaud, J.P.; Horstmann, K.H.; Quast, A. Hybrid laminar fin investigations. In Proceedings of the ONERA/DLR Aerospace Symposium, Paris, France, 21–24 May 1999.
18. Geng, Z.; Liu, S.; Wang, X.; Zhang, Y. Experimental study on drag reduction technology of two-dimensional airfoil mixed laminar flow control. *J. Exp. Fluid Mech.* **2010**, *24*, 46–50. (In Chinese)
19. Wang, F.; Eriqitai; Wang, Q.; Guo, H.; Su, P. Experiment on mixed laminar flow control mechanism of swept wing. *Acta Aerodyn. Sin.* **2010**, *25*, 918–924. (In Chinese)
20. Shi, Y.; Cao, T.; Yang, T.; Bai, J.; Qu, F.; Yang, Y. Estimation and analysis of hybrid laminar flow control on a transonic experiment. *AIAA J.* **2020**, *58*, 118–132. [CrossRef]
21. Scholz, P.; Barklage, A.; van Rooijen, B.; Seitz, A.; Horn, M.; Badrya, C.; Radespiel, R. Large-scale wind tunnel testing of an advanced hybrid laminar flow control system. In Proceedings of the AIAA Aviation Forum, Chicago, IL, USA, 27 June–1 July 2022; p. 3371.
22. Mery, F.; Piot, E.; Forte, M.; Aguilar, B.; Godard, J.L.; Bardoux, P. Hybrid laminar flow control investigation of microperforated skin with variable porosity suction device. In Proceedings of the AIAA SCITECH 2025 Forum, Orlando, FL, USA, 6–10 January 2025.
23. Zhao, Y.; Duan, Z.; Ding, X.; Yang, T.; Wang, M. Optimization design of mixed laminar wing for flight test. *Acta Aeronaut. Astronaut. Sin.* **2022**, *43*, 157–170. (In Chinese)
24. Zhu, Z. *Prediction Method and Application of Transition Around Complex Shape of Aircraft [D]*; Northwestern Polytechnical University: Xi'an, China, 2022. (In Chinese)
25. Shi, Y.; Lan, X.; Yang, T. Hybrid laminar flow control optimizations for infinite swept wings. *Int. J. Aerosp. Eng.* **2023**, *2023*, 3455238. [CrossRef]
26. Sudhi, A.; Radespiel, R.; Badrya, C. Design exploration of transonic airfoils for natural and hybrid laminar flow control applications. *J. Aircr.* **2023**, *60*, 1–15. [CrossRef]
27. Langtry, R.B.; Menter, F.R. Correlation-based transition modeling for unstructured parallelized computational fluid dynamics codes. *AIAA J.* **2009**, *47*, 2894–2906. [CrossRef]
28. Wright, M.C.M.; Nelson, P.A. Wind tunnel experiments on the optimization of distributed suction for laminar flow control. *Proc. Inst. Mech. Eng. Part G J. Aerosp. Eng.* **2001**, *215*, 343–354. [CrossRef]
29. Keith, K.; Crawford, M.E. *Convective Heat and Mass Transfer*; Science Press: Beijing, China, 1986. (In Chinese)

Disclaimer/Publisher's Note: The statements, opinions and data contained in all publications are solely those of the individual author(s) and contributor(s) and not of MDPI and/or the editor(s). MDPI and/or the editor(s) disclaim responsibility for any injury to people or property resulting from any ideas, methods, instructions or products referred to in the content.